ORCA – Online Research @ Cardiff

Citation for final published version:

Munoz-Herrera, Claudio, Aravind, B, Rojas, Paula, Hernández, Christian, Mashruk, Syed, Valera-Medina, Agustin and Toledo, Mario 2026. Analysis of ammonia–methane stabilized flames in an optically accessible porous media burner through chemiluminescence imaging. Fuel: The Science and Technology of Fuel and Energy 412 , 138122. 10.1016/j.fuel.2025.138122

Publishers page: https://doi.org/10.1016/j.fuel.2025.138122

Full-length article

Analysis of Ammonia–Methane Stabilized Flames in an Optically Accessible Porous Media Burner through Chemiluminescence Imaging

Claudio Munoz-Herrera[a], B Aravind[b], Paula Rojas[a], Christian Hernández[a], Syed Mashruk[b], Agustin Valera-Medina[b], Mario Toledo[a*]

[a] Department of Mechanical Engineering, Universidad Técnica Federico Santa María, Av. España 1680, Valparaíso, Chile.

[b] College of Physical Sciences and Engineering, Cardiff University, Wales, UK.

[*]Corresponding author. Email: mario.toledo@usm.cl

Abstract

Porous media burners (PMBs) offer enhanced combustion efficiency and extended stability limits through heat recirculation, yet their limited optical accessibility has restricted experimental insight into pore-scale flame behavior. In this study, methane–ammonia premixed flames were investigated in a two-zone PMB with a downstream bed reduced to a single-sphere thickness to provide enhanced optical access. OH^* and NH^* chemiluminescence imaging was used to visualize interphase-stabilized flame fronts across equivalence ratios of 0.7–1.0, mass fluxes of 0.2–0.4 kg m^{-2} s^{-1}, and ammonia fractions up to 50% by volume in the fuel mixture. Stability maps showed that pure methane flames stabilized only at the highest mass flux, whereas increasing NH_3 content displaced the flashback region toward lower mass fluxes and introduced blow-out or extinction zones under lean or low-reactivity conditions. A first-order stability indicator, defined using the ratio of filtration velocity to laminar flame speed, qualitatively delineated the stability regimes with 86% overall accuracy. Chemiluminescence images revealed different stabilized flame-front morphologies which are proposed as a mean to explain mechanisms that are expected to be present simultaneously in conventional two-zone PMBs. These patterns reflect the complex thermochemistry inside the intricate geometries of PMBs. While conventional packed-bed burners may exhibit further distorted flame morphologies, this study provides valuable insights for advancing the understanding of pore-level combustion in PMBs.

Keywords: Flame stabilization analysis, filtration combustion, ammonia, fuel blending, porous media burners.

1 Introduction

Porous media burners (PMBs) have gained attention as a promising clean combustion technology. In these reactors, combustion occurs within a chemically inert but thermally active solid phase [1], allowing heat from the hot products to be transferred upstream through conduction and radiation to preheat the fresh premix [2]. This results in increased characteristic chemical speeds, extended flammability limits and improved efficiency in burning low-heating-value fuels [3]. Due to these advantages, PMBs have been widely explored for various applications, including power generation, high-temperature heat production, residential appliances and fuel reforming [4–7]. To maintain stable operation and prevent undesired flame displacement [8,9], most PMB designs incorporate flame front stabilization techniques, such as variations in pore size in two-zone burners [7,10,11] or the use of a variable cross-section [12–14].

However, a fundamental challenge in conventional PMBs is the lack of optical accessibility to the reaction zone. The porous matrix, as well as the burner structure, blocks almost all direct visualization, making it difficult to obtain spatially resolved data on pore-level flame structure. As a result, most experimental studies have relied on intrusive measurements, such as thermocouples for temperature profiling or gas analyzers for exhaust composition analysis, which provide limited insight into the complex pore-scale combustion dynamics. Advanced optical diagnostic techniques have been employed to overcome these limitations, yet these methods introduce trade-offs between optical accessibility and experimental fidelity.

Several researchers have attempted to visualize combustion within PMBs by modifying burner designs or employing novel measurement techniques. Stelzner et al. [15] investigated the flame structure in lean methane-air combustion within porous inert media using laser-induced fluorescence (LIF) to visualize the distribution of hydroxyl (OH) radicals, as a marker for the flame front. The porous burner consisted of a SiSiC foam structure with a cross section of 135 x 185 mm^2,a height of 15 mm, and 10 pores per inch (PPI), which was sliced and placed together over an alumina flame trap, leaving small channels with widths of the order of pore diameters to generate paths for the lasers between the foam slices. Since the measures could be made only for the gas phase, no clear images of flame-solid interaction or flame front morphology could be obtained, and the local conductive and radiative heat transfer processes were altered. The study revealed that the position of the maximum OH concentration is almost independent of the equivalence ratio at constant thermal load and that the flame zone length decreases as the equivalence ratio is reduced. They found that for lower equivalence ratios and firing rates (200 kW m^{-2}), the flame stabilized near the flame trap, while for the highest firing rates (800 kW m^{-2}) the flame front moves downstream until it reaches the blow-off region. Between those regimes, the flame front remains nearly in the same location, which is one of the advantages of PMBs.

Boigné et al. [16] developed a new experimental diagnostic method that simultaneously combines synchrotron X-ray micro-computed tomography (μCT) and short-wavelength infrared thermometry to measure the solid's surface and 3-D gas phase temperature with micrometric resolution. The burner employed consisted of a quartz cylinder without thermal insulation which held a 3-D printed SiSiC porous matrix based on the periodic repetition of the elemental structure of a Kelvin cell, with pores comparable to 10 PPI. By employing high concentrations of Krypton to enhance X-ray attenuation through the gas to enable gas-phase μCT temperature measurements, this method allowed for unique analysis of the pore-level combustion process. Finger-like flames were observed and associated with the distribution of fresh gases into the burner. The authors determined that nearly 80% of the combustion process takes place in an adiabatic preheated flamelet regime, with the effects of heat transfer between phases affecting only to 20% of the reacting zone.

Flores-Montoya et al. [17] used a 3-D printed computer-generated geometry with incorporated see-through directions to track a CH_4-air flame front using CH^* chemiluminescence. Burners with pore sizes going from 1.5 mm to 3.5 mm were considered. The authors found nearly one-dimensional flame front featuring a thickened reaction region, based on CH^* and temperature measures. Contrast with state-of-the-art volume-averaged models were performed, recognizing discrepancies in the location and thickness of the heat release zone and a high-sensitivity to the heat exchange coefficient between phases. On a following investigation, using a similar reactor with optically-accessible pathways, Flores-Montoya et al. [18] employed Mie-scattering imaging and micro particle imaging velocimetry (μPIV) to study heat recirculation and determine 2-D flow fields inside the burner using CH_4-H_2 mixtures as fuel. Symmetric and asymmetric stabilization modes were observed through both Mie-scattering and CH^* chemiluminescence, with asymmetric stabilization being promoted when the H_2 content increased. Combining Mie-scattering with μPIV, it was possible to determine local consumption speeds of several flames, recognizing that the flame surface increases to accommodate larger mass flows.

Given the capability of PMBs to burn low-heating-value fuels with high efficiency and reduced emissions [19], researchers have investigated their use for ammonia (NH_3) combustion. Ammonia is considered a promising energy carrier for the current energy transition due to its high hydrogen density, well-established production infrastructure, and ease of storage and transport compared to hydrogen [20–22]. However, NH_3 presents significant combustion challenges, including low heating value (37% of CH_4), slow laminar burning velocity (7 cm s^{-1} vs. 38 cm s^{-1} for CH_4), and high minimum ignition energy (nearly 30 times that of CH_4) [23]. Moreover, ammonia combustion is prone to NO_x and unburnt NH_3 emissions, and it presents narrow flammability limits compared to fossil fuels requiring innovative combustion strategies to improve its feasibility [24].

Given these challenges, PMBs have shown to be a promising pathway to enable stable ammonia combustion. Vignat et al. [25] showed that PMBs can operate on pure ammonia with emission levels comparable to gas turbine burners, and while maintaining larger firing ratios and power densities than swirl flames. These findings highlight the potential of PMBs to unlock ammonia's energy potential, yet a fundamental understanding of the combustion process at the pore-scale remains lacking.

The need for detailed experimental investigations at the pore-scale has become increasingly critical with the rapid development and adoption of direct pore-level simulations (DPLS). While computational power has enabled more sophisticated modeling approaches, significant discrepancies between DPLS and conventional volume-averaged models (VAMs) have been reported, as discontinuities in the flame front, flame wrinkling and localized heat recirculation are not well captured in VAMs which lead to inaccuracies in predicted burning rates, temperature fields and reaction rates [26,27]. A lack of experimental data to compare DPLS results is still present, as local flame front morphology and its distribution inside a porous media reactor is still largely unknown. Additionally, the existing literature on stabilized flame front morphology has focused on hydrocarbon [17] or hydrocarbon-H_2 [18] flames, without considering flames with slower chemistry, such as ammonia containing mixtures.

This study presents an experimental investigation of interphase-stabilized CH_4-NH_3 flames in a one-layer porous media burner with enhanced optical access. The goals of this work are the following: (a) Identify stability regimes in the employed burner and evaluate how they evolve as NH_3 concentration in the fuel mixture increases, (b) Propose a predictor for the a-priori identification of stable operational regimes, and (c) Provide novel images of pore-level flame structures using chemiluminescence imaging, offering insights into flame front morphology inside PMBs. To the best of the authors' knowledge, this study presents the first experimental observations of interphase-stabilized flame fronts including NH_3 as fuel in a packed-bed PMB using chemiluminescence, which allows for a better understanding of the pore-level combustion process inside PMBs.

The remainder of this paper is structured as follows: Section 2 describes the experimental set-up and methods employed, Section 3 presents the results of this investigation, namely, stability maps, a proposed predictor stability regime identification, classification of stable flame fronts found, an analysis of finger-like flames recognized under stable conditions and finally, comments on the use of NH^* as a flame marker. Section 4 presents the conclusions of this work.

2 Methodology

2.1 Experimental set-up

Figure 1 shows a schematic of the experimental set-up considered for the present study. A one-layer-thickness porous media burner, based on the design proposed in [28], was employed to investigate the stability regimes and flame-front structure of CH_4-NH_3-air mixtures under various operational conditions. The burner consisted of two parallel stainless-steel plates (300 × 115 mm^2), separated by stainless steel spacers that maintained a constant 7 mm gap between them. The plates were bolted together and sealed to prevent gas leakage. Each plate featured a rectangular quartz window (160 × 50 mm^2), providing optical access for high-resolution imaging of the stabilized flames inside the reactor, while the premixed reactants were introduced at the bottom of the burner. This configuration provides easy opticall access to flame fronts, while keeping key characteristics of interphase-stabilized flames in packed bed burners, such as random arrangement of pebbles, steep change in pore size at the interphase and unit cells in the order of the larger pebble size for the development and study of pore-level flames. Heat losses were reduced by covering the whole burner, with exception of the window shown in red dashed line on Figure 1 with a 5 cm layer of thermal insulation wool.

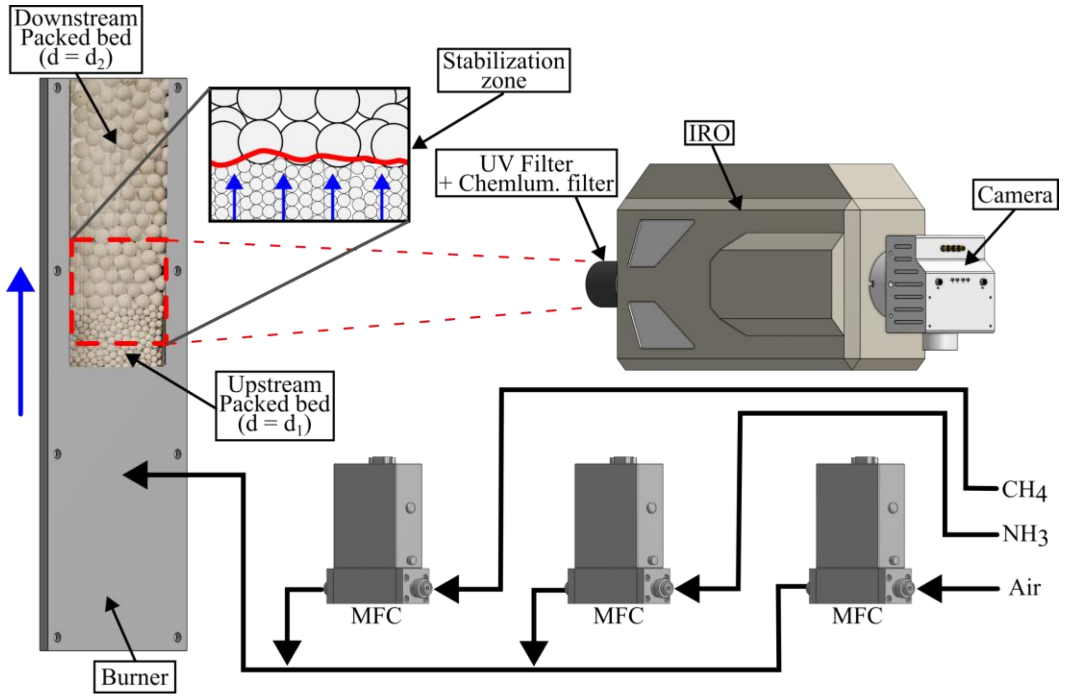

Figure 1: Schematic representation of the experimental set-up employed in the present study. The blue arrow indicates the direction of the flow inside the burner and the dashed red square represents the stabilization zone where the images were taken. The burner is shown uninsulated; however, it was fully covered by a 5 cm layer of thermal insulation wool, excepting the stabilization zone.

Alicat (Tucson, AZ, USA) mass flow controllers (MFCs) were used to precisely regulate the flow rates of both fuel and air, with an accuracy of ± 0.02 SLPM. The parametric space considered was characterized in terms of the equivalence ratio (ϕ), the mass flux ($\dot{m}''$), and the ammonia fraction in the fuel mixture (α), calculated as

$$\phi = \frac{(Fuel/Air)}{(Fuel/Air)_{Stoichiometric}}, \tag{1}$$

$$\dot{m}'' = \frac{\dot{V}}{A_{CS}}\rho_g \ , \tag{2}$$

$$\alpha = \frac{\dot{V}_{\mathrm{NH_3}}}{\dot{V}_{\mathrm{NH_3}}+\dot{V}_{\mathrm{CH_4}}}, \tag{3}$$

where $\dot{V}$ corresponds to the premix volumetric flow rate, A_{CS} to the cross-sectional area of the burner, and ρ_g to the gas phase density. The study considered $\phi \in \{0.7, 0.8, 0.9, 1.0\} \pm 0.025$, $\dot{m}'' \in \{0.2, 0.3, 0.4\}$ kg m^{-2} s^{-1} ± 0.002 kg m^{-2} s^{-1}, and $\alpha \in \{0.0, 0.3, 0.5\} \pm 0.01$.

Inside the reactor, alumina (Al_2O_3) spheres were used to create two distinct packed beds, which promote flame stabilization near the interphase between both zones due to the change in pore size [29,30]. The upstream zone was packed with spheres with a diameter d_1 = 2.5 mm over a length of 175 mm, while the downstream zone contained spheres with a diameter d_2 = 5.6 mm over a length of 85 mm. This arrangement provided a clear distinction between both porous zones, although, upstream pebbles manage to accommodate to downstream spheres, capturing to a certain degree the complex interphase of regular 2-zones packed bed burners. Pebble diameters employed were selected as they are similar or equal to others used in several experimental studies for porous media combustion [12,13,31–36]. Due to elevated heat losses through the structure of the burner after ignition, the burner was fully insulated, leaving only an optical window for image acquisition to promote the transition from surface to submerged-flames [37].

The chemiluminescence images of the flames were captured using a Phantom VEO 710L/S high-speed CMOS camera (Wayne, New Jersey, USA), coupled with a LaVision high-speed intensifier (Göttingen, Germany), was used for the chemiluminescence imaging, as it has been done in [38,39]. The camera gate width was set to 35 ms, and 400 images were acquired at a frequency of 100 Hz. The chemiluminescence signals from OH^* (309 nm; $A^2\Sigma^+ - X^2\Pi$ system), and NH^* (336 nm; $A^3\Pi - X^3\Sigma^-$ system) were collected using bandpass filters (±10 nm FWHM) [40].

2.2 Experimental procedure

The burner was ignited using pure CH_4 ($\alpha = 0.0$), with a mass flux of 0.4 kg m^{-2} s^{-1} and ϕ = 1.0. This condition allowed the flame front to move upstream until it stabilized at the interphase between both packed beds. Once the flame reached this region, the premix composition was adjusted according to each specific test case. A 20-minute stabilization period was maintained for each condition to ensure steady-state operation. Considering that flame front velocities are ~1 mm min^{-1}, even for one-layer-thickness reactors [28], this time should be enough to detect flame front propagation in any direction. During this period, the reaction front was continuously monitored using OH* chemiluminescence imaging.

Unstable conditions such as flame blow-out and flashback correspond to the steady displacement of the flame front downstream and upstream, respectively, from the interphase between both packed beds. If the chemical heat release was not enough to sustain the combustion process, flame extinction was observed. If neither of the previous conditions was met, the operating condition was considered stable and OH*-NH* chemiluminescence images were taken, before moving to the next condition.

2.3 Image postprocessing

For each stable condition, high-speed imaging at 100 Hz was conducted over an integration time of 4 s, using LaVision Davis v10. Each dataset underwent post-processing, including background subtraction, time-averaging over the integration period, and application of a median filter (3 × 3 pixel^2 window) to reduce noise, following [39], and then normalized to their maximum value. A representative processed image is shown in Figure 2. The line marked in green in .a and both its parallel neighboring lines are shown in gray in Figure 2.b, where the filtered signal appears in red.

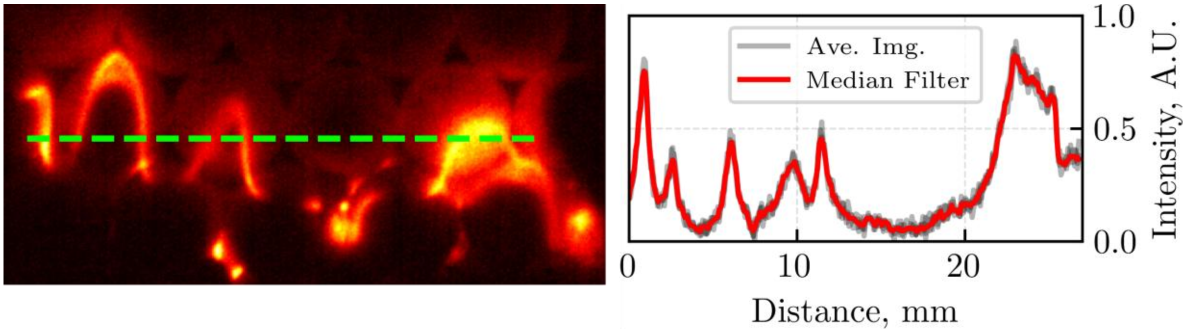

(a) (b)

Figure 2: Example of median filter application. (a) NH^* image obtained for case $\phi = 0.7$, $\dot{m}'' = 0.4$ kg m^{-2} s^{-1}, and $\alpha = 0.0$. (b) Comparison between the values obtained after the averaging over the integration time and the values obtained after the median filter is applied. The green dashed line in (a) marks the position where data for (b) is extracted.

3 Results and discussion

3.1 Stability maps

In porous media combustion, when the flame characteristic length is much smaller than the reactor's length, four distinct regimes can be identified: (1) steady flashback, (2) stable flames, (3) steady blow-out, and (4) flame extinction. Since the flame stabilization process can be thought of as a local balance between physical and chemical velocity, as a reference, Figure 3 presents laminar flame speeds (S_L) for all cases studied. These values were obtained using Cantera [41] with the CRECK mechanism for C_1-C_3-NH_3 mixtures [42,43].

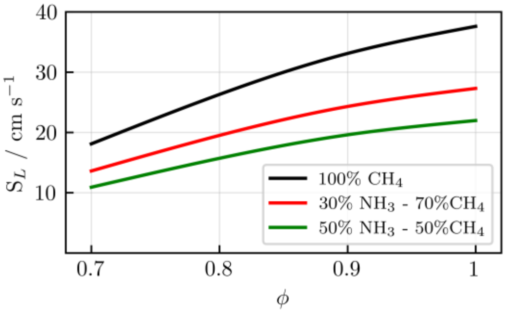

Figure 3: Laminar flame speed for all cases considered in the present study, obtained numerically using Cantera.

Through the present investigation it is demonstrated that change in pore-size, which is the base for two-zone PMBs can be employed in one-layer PMBs to stabilize flames. Based on the experimental tests performed, the stability maps obtained for all tested conditions are shown in Figure 4, as a function of ϕ, $\dot{m}''$ and α. In general, as ammonia is added to the mixture, the stable operating zone is displaced into lower mass fluxes, due to the reduction in flame speed depicted in Figure 3. Wider stable operating zones have been reported in the literature for fully insulated porous media reactors [10,25], however, the registered trends and qualitative behavior are still physically meaningful.

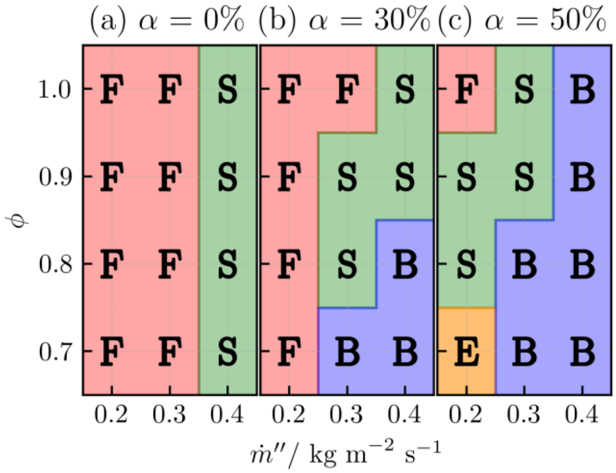

Figure 4: Stability maps as a function of mass flux and equivalence ratio for different α values; The tested conditions are labeled as follows: (1) F: Flashback; (2) S: Stable Flame; (3) B: Flame Blow-out; (4) E: Flame Extinction.

For the baseline case ($\alpha = 0$), stable operation is observed only at the highest mass flux tested, i.e., 0.4 kg m^{-2} s^{-1} across all equivalence ratios, which is consistent with relatively high S_L values for pure methane. At lower mass fluxes, the flame propagated into the upstream porous media, leading to steady flashback, as the chemical velocity exceeds the physical speed of the flow. For α = 30%, the flashback limit was displaced to lower mass fluxes. Flashback was observed at $\dot{m}''$ = 0.2 kg m^{-2} s^{-1} for all ϕ tested, and at $\dot{m}''$ = 0.3 kg m^{-2} s^{-1} for ϕ = 1.0. For $\dot{m}''$ = 0.3 kg m^{-2} s^{-1}, two stable conditions are identified for $\phi \in \{0.8, 0.9\}$, while the stable zone at 0.4 kg m^{-2} s^{-1} for $\phi \in \{0.9, 1.0\}$ remained unchanged with respect to the $\alpha = 0$ case. For leaner mixtures at high mass flux, a flame blow-out zone was registered. At ϕ = 0.7, S_L decreases by 25% when α increases from 0% to 30%, possibly explaining the flame's inability to remain anchored at higher flow velocities. For α = 50%, the stable region shifted to lower mass fluxes, achieving stability at $\dot{m}''$ = 0.2 kg m^{-2} s^{-1}. Under these conditions, flame extinction occurred for the leanest mixture tested, as the chemical heat release was insufficient to sustain combustion. At the same mass flux, but under stoichiometric conditions, flashback was registered. The transition from flame extinction to stable flames to flashback at constant $\dot{m}''$= 0.2 kg m^{-2} s^{-1}, as the equivalence ratio increases, can be explained by the subsequent increase in thermal power and S_L. Additionally, the flame blow-out zone expanded toward richer conditions, reaching stoichiometric levels at the highest mass flux tested, which is associated with the significant reduction in S_L observed in Figure 3, as α increases.

3.2 A first-order stability indicator based on reduced inlet velocity

Historically, the determination of the limits of stable operation in porous media burners has been done through brute-force experimental testing [17,25]. The stability trends observed in Figure 4 suggest that the balance between the characteristic physical velocity of the incoming reactants and the chemical reactivity of the mixture plays an important role in determining whether the flame front remains anchored at the interphase, propagates upstream, or is pushed downstream. Motivated by this physical picture, a first-order stability indicator is proposed to explore whether this balance can be used to qualitatively delineate the different operating regimes observed in the present experiments.

Even though in this case the analysis is done a-posteriori, it corresponds to a first step in the development of low-order stability predictors for PMBs.

Chemical velocity can be characterized by the laminar flame speed of the fuel-air mixture, while physical velocity is characterized by the filtration velocity of the premix (u_f), defined as

$$u_f = \frac{\dot{m}''}{\varepsilon\rho_g}, \tag{4}$$

which corresponds to the mean pore-level velocity considering the cross-sectional area reduction caused by the presence of the solid phase. This reduction causes a velocity increase by a factor of $1/\varepsilon$, where ε represents the porosity of the burner, taken as 0.44 for this configuration [28].

The indicator is based on the ratio between the inlet filtration velocity and the laminar flame speed of the corresponding mixture, resulting in a non-dimensional velocity (υ)

$$\upsilon = \frac{u_f}{S_L}. \tag{5}$$

This parameter is of physical significance, as stable operation is achieved when the flow velocity and the local chemical reaction rate are locally balanced within the reactor. While this representation simplifies the velocity fields by reducing them to a single representative value and neglecting effects such as heat losses, thermal expansion, and changes in chemical composition, it can capture trends observed in the stability maps of Figure 4, only using a-priori available information.

Figure 5 presents the inverse of the reduced velocity (υ^{-1}) as a function of mass flux for the three α values tested. Across all conditions, the filtration velocity exceeds the flame speed, resulting in $\upsilon^{-1} < 1$, with values spanning from 0.1 to 0.9. A decreasing trend in υ^{-1} is observed as mass flux increases for all α values. Also, for constant α and $\dot{m}''$, lower υ^{-1} values are recorded for leaner mixtures. Since $\dot{m}''$ is directly proportional to u_f, the observed υ^{-1} curves decrease as $\sim 1/\dot{m}''$, rather than following the linear dependence predicted for $\upsilon(\dot{m}'')$.

Based on the parameter υ^{-1}, intervals that approximate the transitions between regimes in the present dataset are proposed. These intervals correspond to steady flashback, stable flame and flame blow-out/extinction. The last interval has been proposed as a mix of two flame regimes since flame extinction occurred only under one operational condition, making it difficult to determine a limit for a separate interval.

The interval boundaries were selected to minimize misclassified points, considering only their dependence on υ^{-1}. The stable operating zone was found to be $0.3 < \upsilon^{-1} < 0.42$. Within this range, variations in S_L due to heat losses and heat recirculation in the porous medium, would be balanced with the changes in u_f due to the chemical reaction, allowing for the flame front to remain steady. For $\upsilon^{-1} < 0.3$, flame blow-out or extinction occurs, while for $\upsilon^{-1} > 0.42$, steady flashback is predicted. Operating points misclassified by the low-order stability indicator are highlighted in red.

To improve classification accuracy, additional parameters such as thermal power could be incorporated. Since thermal power depends linearly on mass flux, defining curved boundaries between different regions could potentially eliminate all misclassified points, given their location on the map. However, to avoid overfitting, this approach was not pursued.

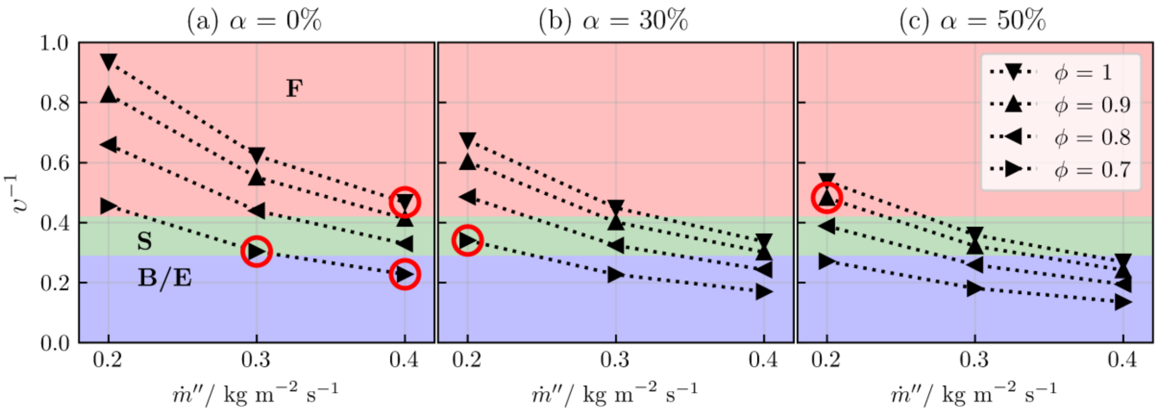

Figure 5: Inverse of reduced velocity as a function of mass flux for different α values. Red, green and blue colored zones correspond to the proposed segments for flashback (F), stable operation (S)

and flame blow-out/extinction (B/E), respectively. Points incorrectly predicted by the proposed segments are circled in red.

A confusion matrix is shown in Figure 6, following [44], depicting the contrast between observed and predicted regimes. Using this single parameter, 86% of the data can be correctly classified, showing that the competition between physical and chemical velocity accounts for a large proportion of the mechanism behind flame stabilization in the studied configuration.

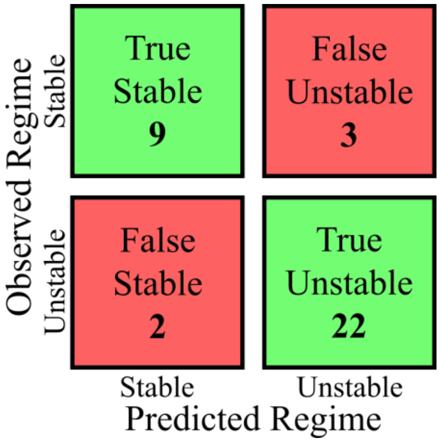

		Predicted Regime	
		Stable	Unstable
Observed Regime	Stable	True Stable **9**	False Unstable **3**
	Unstable	False Stable **2**	True Unstable **22**

Figure 6: Confusion matrix for the proposed prediction model.

It is important to note that the stability zones and the limiting υ^{-1} values identified in this study are specific to the experimental conditions and could vary significantly in a well-insulated burner, for different porous media configurations or for different fuels. For example, Ferguson et al. [45] reported a transition between stable operation and flashback at $\upsilon^{-1} \approx 0.2$ in a direct pore-level simulation with 70% porosity and no heat losses to the environment. This value is approximately 50% lower than the $\upsilon^{-1} = 0.42$ identified in this study, highlighting the strong dependence of stability limits on burner configuration and solid-phase thermal conduction. Despite such variations, the development of low-order predictors remains valuable for a-priori estimation of stability regimes in porous media combustion.

3.3 Types of stable flame fronts observed

Shared morphological characteristics observed across the twelve stable operating conditions motivated the identification of three predominant flame-front patterns. These patterns should not be interpreted as rigid categories, but rather as recurring behaviors that emerged within the specific configuration and operating space studied. The observed morphologies include:

(1) interphase-stabilized flame fronts with finger-like structures (FL),

(2) canonically interphase-stabilized flame fronts (C), and

(3) flame fronts exhibiting a sustained inclination (I).

Each pattern highlights different ways in which pore-level flow distribution, solid geometry, and mixture reactivity may influence front anchoring within the burner. The FL flame fronts observed are characterized by the presence of elongated finger-like structures which exhibit a length in the order of d_2. C flame fronts, named after the ideal construct of a thin, ordered flame front placed at the interphase between both packed beds, exhibits no major distortions on pore-level flames, with flame lengths in the order of d_1. Finally, I flame fronts are characterized, as the name suggest, by an inclination of the flame front that was sustained over the sampling time and that, for the conditions tested in this study can reach up to 17° of inclination.

Figure 7 presents a simplified version of the stability maps from Figure 4, displaying only the stable operating conditions identified, detailing the corresponding typo of flame front observed for each case. In some instances, characteristics of two flame classes were simultaneously present, so both classifications are indicated in the maps using a slash notation. Furthermore, the υ^{-1} values shown in parentheses exhibit no clear correlation with the flame morphology, reinforcing that this parameter captures regime stability but not structural details of the stabilized front.

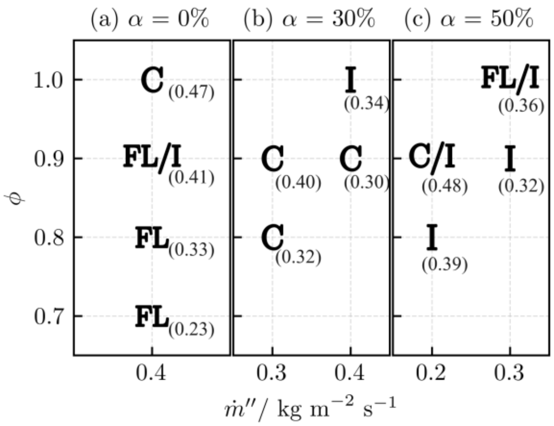

Figure 7: Morphological classification of stable flame fronts found in the present study for (a) α = 0%, (b) α = 30%, and (c) α = 50%. Abbreviations correspond to Canonically interphase-stabilized flame fronts (C), Interphase-stabilized flame fronts with finger-like structures (FL) and Inclined stabilized flame fronts (I). For cases where a mixture of two categories is observed, both are indicated separated by a slash. Values of υ^{-1} are presented in parentheses for each case as a reference.

3.3.1 Interphase-stabilized flame fronts with finger-like structures

For α = 0%, FL-type flames were the most frequently observed pattern. This type of flames have been observed in direct pore-level simulations for different burner configurations [26,45]. As discussed by Sirotkin et al. [46], in the stable regime, in regions with high local velocity, the premixed reactants require more time to preheat before ignition, which leads to flame front distortions and the formation of finger-like structures. The dominance of FL-type flames for pure methane is associated to the higher mass fluxes required for stabilization, i.e. 0.4 kg m^{-2} s^{-1}, which was the highest among all test cases. In fact, under stoichiometric conditions, close to peak laminar flame speed, at the same mass flux, a C flame front is observed, due to increased chemical velocity, supported by the increasing υ^{-1} values as ϕ increases. Considering the flashback limit for α = 0% and the presence of elongated flames in this regime, it is proposed that the stabilization is mainly achieved due to higher mass fluxes that remove heat from the upstream packed bed at a rate high enough to avoid the flame front propagating into the smaller pore size section. This, however, promotes pore-level flames being elongated and distorted under conditions where the chemical characteristic velocity is smaller than the physical one.

Figure 8 presents OH^* and NH^* chemiluminescence images for an FL flame front. Nearly the entire flame front is located over a distance d_2 above the interphase, except for small pockets of flames enclosed in circles. The flame front is discontinuous, composed of unitary pore-level flames, which are non-uniformly distributed and exhibit different morphologies. A collection of finger-like flames is shown enclosed in a rectangle, which, even though they have different lengths and tip curvature, exhibit characteristic lengths and widths on the order of d_2. This difference is attributed to the complex internal geometry of the packed bed and subsequent premix distribution, which generates differences even between neighboring unitary flames. A unitary finger-like flame distorted by these effects is pointed by an arrow in the Figure.

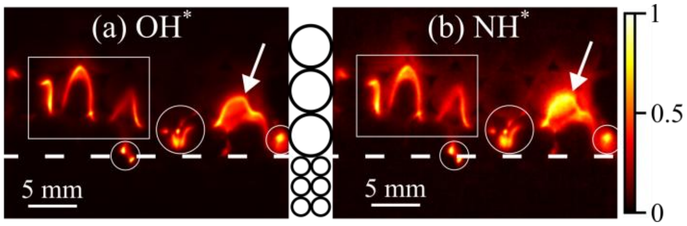

Figure 8: (a) OH^* and (b) NH^* chemiluminescence images of an interphase-stabilized flame front with finger-like flames, particularly for the case ϕ = 0.7, $\dot{m}''$ = 0.4 kg m^{-2} s^{-1} and α = 0%. A dashed line to point the location of the interphase and circles with diameters d_1 and d_2 are added as a reference.

3.3.2 Canonically interphase-stabilized flame fronts

At α = 30%, most of the stable conditions displayed a flame front morphology resembling the idealized behavior expected for two-zone PMBs, i.e., a nearly one-dimensional flame front located right at the interphase between both packed beds. Due to this, they are referred to as canonically interphase-stabilized flames (C), with the caution that deviations from idealized behavior are present. The term canonical has been employed for this type of flame front as it is what would be theoretically expected to occur at the interphase between both packed beds, given the explanations of flame front stabilization present in the literature [29,47]. The more uniform characteristics of unitary flames observed in this regime is associated with the drive of the flame front to propagate into the upstream packed bed, while being continuously quenched [47]. In this way, similar small flame structures are observed across the flame front, as their location and shape are predominantly influenced by the upstream section, where a more uniform packing is present. This morphology is also observed for the case ϕ = 1.0, $\dot{m}''$ = 0.4 kg m^{-2} s^{-1}, and α = 0%.

Figure 9 shows chemiluminescence images of OH* and NH* for a C flame front, for the case ϕ = 0.9, $\dot{m}''$ = 0.3 kg m^{-2} s^{-1} and α = 30%. Despite a relatively uniform reaction zone, the random packing arrangement in the porous domain introduces a complex intensity distribution across the interphase, with coincident hot spots observed for both radicals, which are pointed out using arrows. Small finger-like structures are still present but appear less frequently and with lengths and widths in the order of d_1, as it is the case of the unitary flame enclosed in a rectangle. Additionally, some small-scale flames penetrate the upstream porous zone, though they do not propagate beyond a distance d_1 from the interphase. These flames, enclosed in ellipses, are continuously quenched, unable to preheat the upstream solid sufficiently for sustained upstream propagation [29,30], which explains their low intensity.

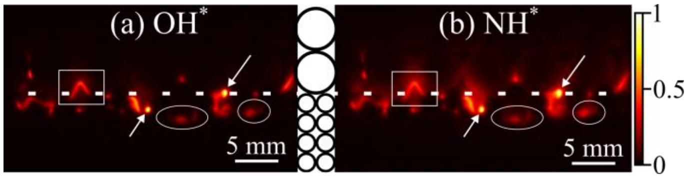

Figure 9: (a) OH* and (b) NH* chemiluminescence images of a canonically interphase-stabilized flame front, particularly for the case ϕ = 0.9, $\dot{m}''$ = 0.3 kg m^{-2} s^{-1} and α = 30%. A dashed line to point the location of the interphase and circles with diameters d_1 and d_2 are added as a reference.

A close-up view for a C-type flame front is shown in Figure 10 for the case ϕ = 0.9, $\dot{m}''$ = 0.4 kg m^{-2} s^{-1} and α = 30%, to facilitate the observation of the flame structure near the interface. Small finger-like flames are observed at the left side of the image enclosed in circles. The one near the corner corresponds to a finger-like flame located on the opposite side of the burner, allowing only the tip of the flame to be visible. As it can be seen on the NH* image, the main finger-like flame is generated exactly in between two d_2 diameter pebbles where there is less resistance to the flow. Right at the interphase and at most a distance d_1 upstream from it, intense flames are observed, which are pointed out using arrows in the Figure. Following a parcel of fluid, in a Lagrangian view, after crossing the preheating zone of the burner, near the interphase is the first location where the heat losses and possibly wall-radical quenching drop below the threshold necessary to promote ignition, as the pore size increases due to changes in the packing. In this way, unitary flames in the order of d_1 are generated after being preheated via heat recirculation. Their location would be mostly influenced by the packing of the reactor, and, as observed in Figure 10, even for this type of flame fronts a non-uniform distribution of unitary flames is obtained. Some small unitary flames, enclosed in rectangles, can propagate further upstream or ignite earlier, but due to high heat losses they exhibit low intensity.

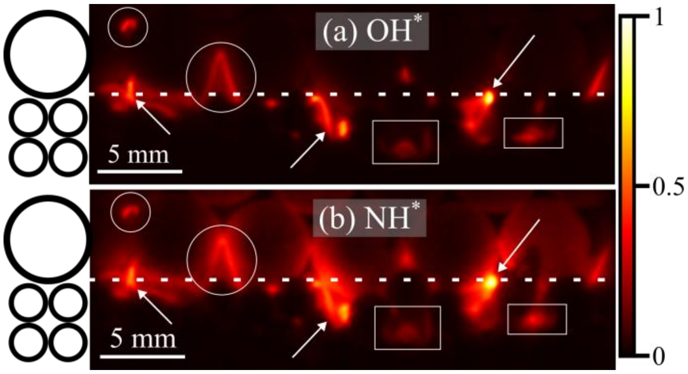

Figure 10: Comparison between (a) OH* and (b) NH* as flame markers for case ϕ = 0.9, $\dot{m}''$ = 0.4 kg m^{-2} s^{-1} and α = 30%. A dashed line to point the location of the interphase and circles with diameters d_1 and d_2 are added as a reference.

3.3.3 Inclined stabilized flame fronts

Finally, for α = 50%, most stable conditions displayed flame fronts with a sustained inclination, here referred to as inclined stabilized (I) flame fronts, where the height difference between the highest and lowest points of the reaction front exceeds d_2. This type of flame front is associated with the lower flame speeds of mixtures with high-ammonia content, thus, making it more sensitive to fluctuations in the velocity field that generate uneven propagation of the flame front until it reaches a local hydrodynamic balance, generating its characteristic inclined morphology. It is worth highlighting that in a fully 3D configuration, this mechanism could generate curved flame fronts. Also, for this ammonia fraction in the fuel mixture, in the leanest condition and for the lowest mass flux, flame extinction was observed due to the inability of the chemical heat release to sustain combustion given the heat losses.

Figure 11 presents chemiluminescence images of OH^* and NH^* for an I-type flame front, particularly for the case ϕ = 0.9, $\dot{m}''$ = 0.3 kg m^{-2} s^{-1} and α = 50%. Based on the definition by Mao et al. [48] , which describes flame front inclination in honeycomb porous burners as the slope of the line connecting its endpoints, the flame front in Figure 11 exhibits an inclination of approximately 17°. Clear discontinuities are observed along the flame front, which are known to occur at low flow rates [28], and, in this case, also at low heating values, due to the high α value considered. Similar inclinations have been observed by Fursenko et al. [28] in a similar burner configuration, where packing variations led to an uneven premix distribution, further contributing to flame front distortions.

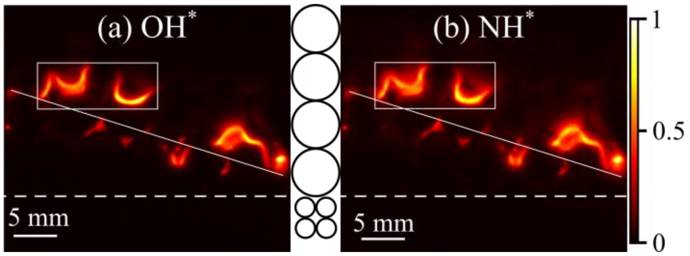

Figure 11: (a) OH* and (b) NH* chemiluminescence images of an inclined stabilized flame front, particularly for the case ϕ = 0.9, $\dot{m}''$ = 0.3 kg m^{-2} s^{-1} and α = 50%. A dashed line to point the location of the interphase and circles with diameters d_1 and d_2 are added as a reference.

As mentioned before, the proposed types of flame fronts are employed only to facilitate the study of the morphologies observed, however they are not universal nor present only one at a time. Figure 12 illustrates a case where FL-, C- and I-type features coexist. Finger-like flames are enclosed in circles, intense small unitary flames right at the interphase are enclosed in a rectangle, and the inclination of the front is highlighted by a dotted line. In this manner, the plausible formation mechanisms for each type of flame front described in the present section can and would be expected to act simultaneously in a conventional PMB. The proposed flame morphologies should be interpreted as emergent trends rather than discrete, universally distinct flame classes.

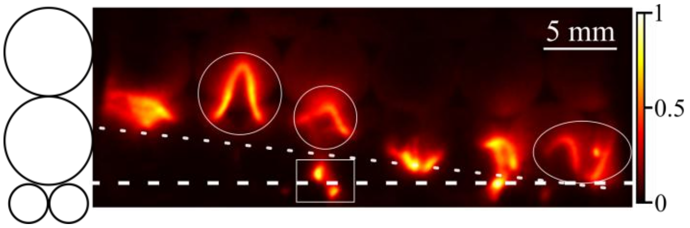

Figure 12: NH* chemiluminescence for the case ϕ = 1, $\dot{m}''$ = 0.3 kg m^{-2} s^{-1} and α = 50%, which exhibits characteristics of both FL and I flame fronts. To clarify the mixed morphology, FL features are enclosed in an ellipse, C features in a rectangle, and I features using a dotted line. A dashed line is added as a reference to mark the location of the interphase.

3.4 Unitary Finger-like flames morphology

Finger-like flames were observed at a consistent spatial location in several stable cases, suggesting the presence of a recurrent flow pattern in the porous structure. Figure 13 collects finger-like flame profiles extracted from a subset of stable flame fronts. Only four cases were excluded, corresponding to three I-class flame fronts and one FL/I mixed flame front, where no finger-like flame was observed in the region of interest. To obtain the profiles shown, the point of highest OH* chemiluminescence intensity along each vertical line was extracted, provided it exceeded a certain threshold. The gray dots in the background represent said discrete points, and to facilitate comparisons among cases, sinusoidal curves were fitted to the data.

The top three curves in Figure 13 correspond to FL-class flame fronts. Although the case ϕ = 1, $\dot{m}''$ = 0.3 kg m^{-2} s^{-1}, α = 50%, is classified as FL/I, its FL-like behavior dominates in the region of interest. As previously discussed, finger-like flames in this stabilization class exhibit an approximate length of d_2, which corresponds to the pebble diameter represented by the dashed blue line. These flames stabilize at a location approximately d_2 further downstream than the rest of the flame profile presented. This displacement could be explained by increased mass flux, which increases the distance needed for the premix to achieve its ignition temperature, shifting the flame downstream.

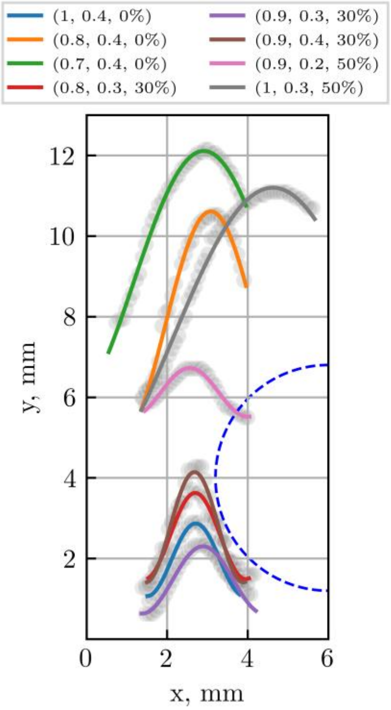

Figure 13: Finger-like flame profiles identified for the studied cases. Profiles are extracted at the same location in each image and are not displaced nor scaled. As a reference, a sinusoidal curve is fitted to the data for each case and the profile of a pebble with diameter d_2 is sketched in dashed line. Cases are labeled in the format $(\phi, \dot{m}'', \alpha)$.

The remaining five flame profiles in Figure 13 correspond to C-class flame fronts or C/I mixed flame fronts, which tend to form at nearly the same location—except for the profile shown in pink, which corresponds to the case with the highest ammonia content. These five profiles are replotted in Figure 14 in a normalized (x*, y*) reference frame, aligning them to a common anchor point for better comparison. Since C-class flame fronts are influenced by the upstream porous zone, the appropriate length scale for comparison is d_1, represented by the half-pebble sketched in green dashed lines.

Across all cases, flame width remains nearly constant, while flame length varies significantly, increasing by a factor of more than two from the shortest (pink curve) to the longest (brown curve) flame. A direct comparison can be made between the brown and purple curves, as they share identical premix compositions, with the only difference being mass flux. As expected, for a constant laminar flame speed, an increase in mass flux reduces the flame cone angle, resulting in a 65% increase in flame length when mass flux rises from 0.3 kg m^{-2} s^{-1} to 0.4 kg m^{-2} s^{-1}.

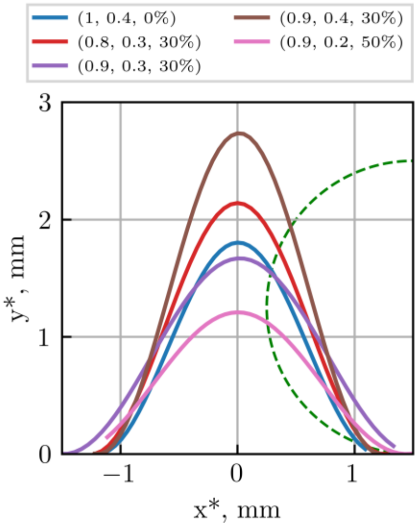

Figure 14: Finger-like flame profiles identified for C class flame fronts. Profiles are translated to facilitate comparison among them. As a reference the profile of a pebble with diameter d_1 is sketched in dashed line. Cases are labeled in the format $(\phi, \dot{m}'', \alpha)$.

3.5 NH* as a flame marker

NH* has been proposed as a flame marker to study NH_3 flames [49,50], role for which OH* is widely accepted when conventional fuels are considered. In this subsection, a comparison between the profiles captured for both excited radicals is performed. To facilitate a qualitative comparison between different cases, a k-means clustering algorithm [51] was applied to the chemiluminescence images obtained for all tested conditions. The results for three representative cases are shown in Figure 15. The optimal number of clusters was determined using the elbow method, based on the normalized inertia for each image, as illustrated in Figure 16, which identified four clusters as the most suitable choice.

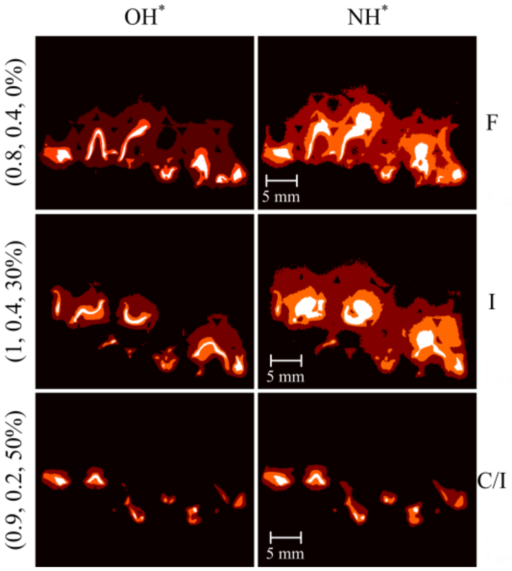

Figure 15: Qualitative comparison among cases with different α values for OH* and NH*, after applying a k-means clustering algorithm, considering k = 4. On the left, cases are labeled using the format $(\phi, \dot{m}'', \alpha)$. On the right the type of stabilized flame front in indicated.

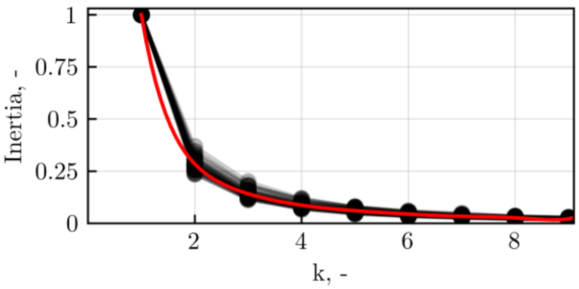

Figure 16: Normalized inertia as a function of the number of clusters, k, for all chemiluminescence images considered in the present study. A polynomial fit is shown in red as a reference.

In Figure 15, the NH_3 fraction in the fuel mixture increases from top to bottom. Across all three cases, OH* highlights well-defined flame structures like those discussed in the previous section. NH* shows a transition in behavior as α increases, shifting from a diffuse distribution to a flame marker role, akin to OH*. For the topmost case (α = 0), the highest-intensity NH* cluster extends over a broad region, however, for the bottommost case (α = 50%), NH* and OH* exhibit only minor differences, suggesting that NH^* can indeed act as a flame marker in methane-ammonia combustion for $\alpha \geq 50\%$. This trend is explained by its formation mechanisms at different ammonia additions: at $\alpha = 0\%$, NH^* originates from air N_2 dissociation, while as α is increased, they primarily result from NH_3 decomposition. Naturally, as NH_3 presence in the fuel mixture is increased, NH^* formed through fuel nitrogen chemistry is increased and its signal correlates better with the flame front position.

4 Conclusions

An experimental investigation of methane–ammonia premixed flames stabilized within a two-zone porous media burner modified to enhance optical access was performed. Using OH^* and NH^* chemiluminescence, pore-scale flame structures were visualized across a range of equivalence ratios, mass fluxes, and ammonia fractions. Stability maps showed clear trends with increasing NH_3 content: the flashback limit shifted toward lower mass fluxes, while blow-out and extinction regions expanded under lean conditions and reduced chemical reactivity. To interpret these limits, a first-order stability indicator based on the ratio of filtration velocity to laminar flame speed was introduced. While derived a posteriori, the indicator captured the qualitative transitions between flashback, stable operation, and blow-out/extinction for 86% of the tested conditions, illustrating the value of low-order predictors for PMB stability assessment.

Chemiluminescence imaging revealed three recurring stabilized flame-front morphologies—finger-like, canonical, and inclined—whose appearance depends on the operating condition and mixture composition. These patterns should be understood as emergent trends rather than discrete, universally distinct flame classes. NH^* chemiluminescence exhibited progressively stronger correspondence with OH^* as NH_3 fraction increased, indicating its potential as a qualitative flame-structure indicator under high-ammonia conditions.

Acknowledgements

The authors would like to thank ANID-Subdirección de Capital Humano/Doctorado Nacional, Chile/2023-21231872, FONDEF ID23I10331, and ANID CTI 250019 Innovation Center for Sustainable Energy Transition (SET-Chile).

Nomenclature

PMB	Porous media burner
PPI	Pores per inch
F	Steady flashback regime
S	Stable flame regime
B	Flame blow-out regime
E	Flame extinction regime
FL	Interphase-stabilized flame fronts with finger-like structures
C	Canonically interphase-stabilized flame fronts
I	Inclined stabilized flame fronts
$\dot{V}$	Volumetric flow rate
A_{CS}	Cross-sectional area of the burner
ρ_g	Gas phase density

S_L	Laminar flame speed
ε	Porosity
d_1	Upstream pebble diameter
d_2	Downstream pebble diameter

References

[1] S. Chalia, M. Naagar, P. Thakur, A. Thakur, S.N. Sridhara, An overview of ceramic materials and their composites in porous media burner applications, Ceramics International 47 (2021) 10426–10441. https://doi.org/10.1016/j.ceramint.2020.12.202.

[2] A.J. Barra, J.L. Ellzey, Heat recirculation and heat transfer in porous burners, Combustion and Flame 137 (2004) 230–241. https://doi.org/10.1016/j.combustflame.2004.02.007.

[3] J.L. Ellzey, E.L. Belmont, C.H. Smith, Heat recirculating reactors: Fundamental research and applications, Progress in Energy and Combustion Science 72 (2019) 32–58. https://doi.org/10.1016/j.pecs.2018.12.001.

[4] D. Mohaddes, C.T. Chang, M. Ihme, Thermodynamic cycle analysis of superadiabatic matrix-stabilized combustion for gas turbine engines, Energy 207 (2020) 118171. https://doi.org/10.1016/j.energy.2020.118171.

[5] G. Coskun, Z. Parlak, O. Yalçınkaya, H. Pehlivan, V. Tür, O. Kosova, Methane-fueled porous burner combustion in a domestic boiler: Experimental and numerical study, Fuel 381 (2025) 133391. https://doi.org/10.1016/j.fuel.2024.133391.

[6] A. Banerjee, D. Paul, Developments and applications of porous medium combustion: A recent review, Energy 221 (2021) 119868. https://doi.org/10.1016/j.energy.2021.119868.

[7] X. Chen, J. Li, X. He, D. Zhao, N. Wang, Experimental and numerical investigation on the performance of meso-scale burners with novel ordered porous media, Applied Thermal Engineering 233 (2023) 121103. https://doi.org/10.1016/j.applthermaleng.2023.121103.

[8] I. Yakovlev, S. Zambalov, Three-dimensional pore-scale numerical simulation of methane-air combustion in inert porous media under the conditions of upstream and downstream combustion wave propagation through the media, Combustion and Flame 209 (2019) 74–98. https://doi.org/10.1016/j.combustflame.2019.07.018.

[9] Y. Wang, X. Chen, H. Ji, T. Li, J. Li, High-resolution dynamic characteristics of thermal wave in porous media burners with low-concentration methane, Energy 313 (2024) 134014. https://doi.org/10.1016/j.energy.2024.134014.

[10] G. Vignat, B. Akoush, E.R. Toro, E. Boigné, M. Ihme, Combustion of lean ammonia-hydrogen fuel blends in a porous media burner, Proceedings of the Combustion Institute 39 (2023) 4195–4204. https://doi.org/10.1016/j.proci.2022.07.054.

[11] J. Shi, M. Mao, H. Li, Y. Liu, J. Lv, A pore level study of syngas production in two-layer burner formed by staggered arrangement of particles, International Journal of Hydrogen Energy 45 (2020) 2331–2340. https://doi.org/10.1016/j.ijhydene.2019.11.017.

[12] C. Munoz-Herrera, O. Skurtys, P. Nikrityuk, R.E. Hayes, M. Toledo, Stabilization of methane–hydrogen flames inside a divergent porous media reactor, Proceedings of the Combustion Institute 40 (2024) 105719. https://doi.org/10.1016/j.proci.2024.105719.

[13] N. Araya, S. Armijo, M. Toledo, Experimental and numerical study of lean combustion of propane in divergent porous media burners, Applied Thermal Engineering 259 (2025) 124710. https://doi.org/10.1016/j.applthermaleng.2024.124710.

[14] P. Qian, M. Liu, X. Li, F. Xie, Z. Huang, C. Luo, X. Zhu, Combustion characteristics and radiation performance of premixed hydrogen/air combustion in a mesoscale divergent porous media combustor, International Journal of Hydrogen Energy 45 (2020) 5002–5013. https://doi.org/10.1016/j.ijhydene.2019.12.094.

[15] B. Stelzner, Ch. Keramiotis, S. Voss, M.A. Founti, D. Trimis, Analysis of the flame structure for lean methane–air combustion in porous inert media by resolving the hydroxyl radical, Proceedings of the Combustion Institute 35 (2015) 3381–3388. https://doi.org/10.1016/j.proci.2014.06.151.

[16] E. Boigné, T. Zirwes, D.Y. Parkinson, G. Vignat, P. Muhunthan, H.S. Barnard, A.A. MacDowell, M. Ihme, Integrated experimental and computational analysis of porous media combustion by combining gas-phase synchrotron μ CT, IR-imaging, and pore-resolved simulations, Combustion and Flame 259 (2024) 113132. https://doi.org/10.1016/j.combustflame.2023.113132.

[17] E. Flores-Montoya, P.-A. Masset, T. Schuller, L. Selle, Flame-front tracking in Porous Media Burners, Combustion and Flame 267 (2024) 113597. https://doi.org/10.1016/j.combustflame.2024.113597.

[18] E. Flores-Montoya, S. Cazin, T. Schuller, L. Selle, Mie-scattering imaging and μ PIV in porous media burners with TPMS-based topologies, Combustion and Flame 274 (2025) 113990. https://doi.org/10.1016/j.combustflame.2025.113990.

[19] K.A. Al-attab, J.C. Ho, Z.A. Zainal, Experimental investigation of submerged flame in packed bed porous media burner fueled by low heating value producer gas, Experimental Thermal and Fluid Science 62 (2015) 1–8. https://doi.org/10.1016/j.expthermflusci.2014.11.007.

[20] A. Valera-Medina, H. Xiao, M. Owen-Jones, W.I.F. David, P.J. Bowen, Ammonia for power, Progress in Energy and Combustion Science 69 (2018) 63–102. https://doi.org/10.1016/j.pecs.2018.07.001.

[21] A. Valera-Medina, F. Amer-Hatem, A.K. Azad, I.C. Dedoussi, M. De Joannon, R.X. Fernandes, P. Glarborg, H. Hashemi, X. He, S. Mashruk, J. McGowan, C. Mounaim-Rouselle, A. Ortiz-Prado, A. Ortiz-Valera, I. Rossetti, B. Shu, M. Yehia, H. Xiao, M. Costa, Review on Ammonia as a Potential Fuel: From Synthesis to Economics, Energy Fuels 35 (2021) 6964–7029. https://doi.org/10.1021/acs.energyfuels.0c03685.

[22] IEA, Ammonia Technology Roadmap, Paris, 2021. https://www.iea.org/reports/ammonia-technology-roadmap.

[23] M. Alnajideen, H. Shi, W. Northrop, D. Emberson, S. Kane, P. Czyzewski, M. Alnaeli, S. Mashruk, K. Rouwenhorst, C. Yu, S. Eckart, A. Valera-Medina, Ammonia combustion and emissions in practical applications: a review, Carb Neutrality 3 (2024) 13. https://doi.org/10.1007/s43979-024-00088-6.

[24] H. Kobayashi, A. Hayakawa, K.D.K.A. Somarathne, E.C. Okafor, Science and technology of ammonia combustion, Proceedings of the Combustion Institute 37 (2019) 109–133. https://doi.org/10.1016/j.proci.2018.09.029.

[25] G. Vignat, T. Zirwes, E.R. Toro, K. Younes, E. Boigné, P. Muhunthan, L. Simitz, D. Trimis, M. Ihme, Experimental and numerical investigation of flame stabilization and pollutant formation in matrix stabilized ammonia-hydrogen combustion, Combustion and Flame 250 (2023) 112642. https://doi.org/10.1016/j.combustflame.2023.112642.

[26] P.-A. Masset, F. Duchaine, A. Pestre, L. Selle, Modelling challenges of volume-averaged combustion in inert porous media, Combustion and Flame 251 (2023) 112678. https://doi.org/10.1016/j.combustflame.2023.112678.

[27] F. Muller, O. Dounia, L. Selle, Direct pore-level simulation of hydrogen flame anchoring mechanisms in an inert porous media, Physics of Fluids 36 (2024) 013336. https://doi.org/10.1063/5.0177131.

[28] R.V. Fursenko, I.A. Yakovlev, E.S. Odintsov, S.D. Zambalov, S.S. Minaev, Pore-scale flame dynamics in a one-layer porous burner, Combustion and Flame 235 (2022) 111711. https://doi.org/10.1016/j.combustflame.2021.111711.
[29] V.S. Babkin, A.A. Korzhavin, V.A. Bunev, Propagation of premixed gaseous explosion flames in porous media, Combustion and Flame 87 (1991) 182–190. https://doi.org/10.1016/0010-2180(91)90168-B.
[30] P.-F. Hsu, W.D. Evans, J.R. Howell, Experimental and Numerical Study of Premixed Combustion Within Nonhomogeneous Porous Ceramics, Combustion Science and Technology 90 (1993) 149–172. https://doi.org/10.1080/00102209308907608.
[31] Z. Ling, L. Lu, X. Zeng, M. Kuang, B. Ling, C. Gao, C. Zhou, Ethylene combustion performance with varying the N2 content in a porous burner, Energy 262 (2023) 125321. https://doi.org/10.1016/j.energy.2022.125321.
[32] H. Wang, C. Wei, P. Zhao, T. Ye, Experimental study on temperature variation in a porous inert media burner for premixed methane air combustion, Energy 72 (2014) 195–200. https://doi.org/10.1016/j.energy.2014.05.024.
[33] Z. Li, H. Dai, C. Zhai, Integrated porous self-sustaining combustion of inert pellets and reactive wood lamellae with additives: Dynamic co-production method for heat and hydrogen, Energy 303 (2024) 131993. https://doi.org/10.1016/j.energy.2024.131993.
[34] S. Panigrahy, S.C. Mishra, The combustion characteristics and performance evaluation of DME (dimethyl ether) as an alternative fuel in a two-section porous burner for domestic cooking application, Energy 150 (2018) 176–189. https://doi.org/10.1016/j.energy.2018.02.121.
[35] M. Liao, Z. He, S. Jia, X. Liang, T.L. Chan, Y. Li, X. Xu, T. Liu, Comparison of the flame stabilities during oxy-methane and air-methane combustion in a two-layer porous burner, Case Studies in Thermal Engineering 51 (2023) 103657. https://doi.org/10.1016/j.csite.2023.103657.
[36] V. Bubnovich, M. Toledo, L. Henríquez, C. Rosas, J. Romero, Flame stabilization between two beds of alumina balls in a porous burner, Applied Thermal Engineering 30 (2010) 92–95. https://doi.org/10.1016/j.applthermaleng.2009.04.001.
[37] M.A. Mujeebu, M.Z. Abdullah, M.Z.A. Bakar, A.A. Mohamad, R.M.N. Muhad, M.K. Abdullah, Combustion in porous media and its applications – A comprehensive survey, Journal of Environmental Management 90 (2009) 2287–2312. https://doi.org/10.1016/j.jenvman.2008.10.009.
[38] B. Aravind, Z. Wang, S. Mashruk, D.A. Lacoste, A. Valera-Medina, Novel strategy for combustion enhancement of NH3-air mixture using gliding arc plasma, Proceedings of the Combustion Institute 41 (2025) 105848. https://doi.org/10.1016/j.proci.2025.105848.
[39] S. Mashruk, E.C. Okafor, M. Kovaleva, A. Alnasif, D. Pugh, A. Hayakawa, A. Valera-Medina, Evolution of N2O production at lean combustion condition in NH3/H2/air premixed swirling flames, Combustion and Flame 244 (2022) 112299. https://doi.org/10.1016/j.combustflame.2022.112299.
[40] A.G. Gaydon, The Spectroscopy of Flames, Springer Netherlands, Dordrecht, 1974. https://doi.org/10.1007/978-94-009-5720-6.
[41] D.G. Goodwin, H.K. Moffat, I. Schoegl, R.L. Speth, B.W. Weber, Cantera: An Object-oriented Software Toolkit for Chemical Kinetics, Thermodynamics, and Transport Processes, (2023). https://doi.org/10.5281/ZENODO.8137090.
[42] Y. Song, L. Marrodán, N. Vin, O. Herbinet, E. Assaf, C. Fittschen, A. Stagni, T. Faravelli, M.U. Alzueta, F. Battin-Leclerc, The sensitizing effects of NO2 and NO on methane low temperature oxidation in a jet stirred reactor, Proceedings of the Combustion Institute 37 (2019) 667–675. https://doi.org/10.1016/j.proci.2018.06.115.
[43] G. Bagheri, E. Ranzi, M. Pelucchi, A. Parente, A. Frassoldati, T. Faravelli, Comprehensive kinetic study of combustion technologies for low environmental impact: MILD and OXY-fuel

combustion of methane, Combustion and Flame 212 (2020) 142–155. https://doi.org/10.1016/j.combustflame.2019.10.014.

[44] T. Zirwes, G. Vignat, E.R. Toro, E. Boigné, K. Younes, D. Trimis, M. Ihme, Improving volume-averaged simulations of matrix-stabilized combustion through direct X-ray µCT characterization: Application to NH3/H2-air combustion, Combustion and Flame 257 (2023) 113020. https://doi.org/10.1016/j.combustflame.2023.113020.

[45] J.C. Ferguson, S. Sobhani, M. Ihme, Pore-resolved simulations of porous media combustion with conjugate heat transfer, Proceedings of the Combustion Institute 38 (2021) 2127–2134. https://doi.org/10.1016/j.proci.2020.06.064.

[46] F. Sirotkin, R. Fursenko, S. Kumar, S. Minaev, Flame anchoring regime of filtrational gas combustion: Theory and experiment, Proceedings of the Combustion Institute 36 (2017) 4383–4389. https://doi.org/10.1016/j.proci.2016.06.006.

[47] D. Trimis, F. Durst, Combustion in a Porous Medium-Advances and Applications, Combustion Science and Technology 121 (1996) 153–168. https://doi.org/10.1080/00102209608935592.

[48] M. Mao, J. Li, J. Li, J. Shi, Y. Liu, F. He, D. Zhou, X. Hou, Numerical study of flame inclination instability in a packed bed with extra lean methane/air intake by an adaptive multi-scale model, Applied Thermal Engineering 239 (2024) 122073. https://doi.org/10.1016/j.applthermaleng.2023.122073.

[49] H. Zhang, X. Han, J. Jiang, X. Li, X. Gan, B. Zhou, Numerical study of experimental feasible heat release rate markers for NH3–H2-air premixed flames, International Journal of Hydrogen Energy 47 (2022) 28165–28175. https://doi.org/10.1016/j.ijhydene.2022.06.124.

[50] C. Chi, S. Sreekumar, D. Thévenin, Data-driven discovery of heat release rate markers for premixed NH 3 /H 2 /air flames using physics-informed machine learning, Fuel 330 (2022) 125508. https://doi.org/10.1016/j.fuel.2022.125508.

[51] A.M. Ikotun, A.E. Ezugwu, L. Abualigah, B. Abuhaija, J. Heming, K-means clustering algorithms: A comprehensive review, variants analysis, and advances in the era of big data, Information Sciences 622 (2023) 178–210. https://doi.org/10.1016/j.ins.2022.11.139.